Ultraslow calorimetric studies of the martensitic transformation of NiFeGa alloys: detection and analysis of avalanche phenomena

José-María Martín-Olalla[1] · Antonio Vidal-Crespo[1] · Francisco Javier Romero[1] · Alejandro F. Manchón-Gordón[2] · Jhon J. Ipus[1] · Javier S. Blázquez[1] · María Carmen Gallardo[1] · Clara F. Conde[1]

Abstract

We study the thermal properties of a bulk $Ni_{55}Fe_{19}Ga_{26}$ Heusler alloy in a conduction calorimeter. At slow heating and cooling rates ($\sim 1\,\mathrm{K\,h^{-1}}$), we compare as-cast and annealed samples. We report a smaller thermal hysteresis after the thermal treatment due to the stabilization of the 14 M modulated structure in the martensite phase. In ultraslow experiments ($40\,\mathrm{mK\,h^{-1}}$), we detect and analyze the calorimetric avalanches associated with the direct and reverse martensitic transformation from cubic to 14 M phase. This reveals a distribution of events characterized by a power law with exponential cutoff $p(u) \propto u^{-\varepsilon} \exp(-u/\xi)$ where $\varepsilon \sim 2$ and damping energies $\xi = 370\,\mu\mathrm{J}$ (direct) and $\xi = 27\,\mu\mathrm{J}$ (reverse) that characterize the asymmetry of the transformation.

Keywords Ultraslow calorimetry · Intermittent dynamics · Avalanches · Heusler alloys

Introduction

TiNi-based alloys are extensively favored in various applications owing to their distinctive shape memory effect and superelasticity [1–3]. Nevertheless, these alloys come with drawbacks such as high cost and a challenging fabrication process [4]. In lieu of these alloys, there has been significant research on Cu-based shape memory alloys due to their cost-effectiveness and comparatively straightforward processing [5–7]. In addition to the conventional thermally induced shape memory effect observed in TiNi-based alloys, Ullakko et al. [8] reported a large magnetic field-induced strain in Ni_2MnGa single crystals. These possible applications are related to the martensitic transformation (MT) that takes place in this kind of materials, a first-order phase transition which occurs in the solid state from a high temperature (high symmetry) austenite phase to a low temperature (low symmetry) martensite phase.

The structure of the martensite phase and the martensitic transformation temperature have been extensively analyzed in NiMn-based Heusler alloys [9, 10], which are very sensitive to both the chemical composition tailoring [11] and the fabrication method [12]. In this sense, the dependence of the valence electron concentration per atom, e/a, is of great significance in the development of Heusler alloys. As an example, the transition temperatures linearly increase with e/a in Ni–Mn–X (X = In, Sn, Ga) systems, i.e., decreasing the X element concentration [13]. On the other hand, it has been shown that the crystal structure of the martensite phase evolves in the sequence $10M \rightarrow 14M \rightarrow L1_0$ with the increase of e/a in Ni–Mn–In system [13].

Although the general formula of Heusler alloys includes Ni, Mn and one element of the Ga, In, Sn or Sb quartet, it has been proposed to replace Mn by Fe in order to improve the mechanical properties [14]. The enhanced ductility of these Ni–Fe–Ga alloys is related to the precipitation of the secondary $\gamma-$phase. In contrast to the compositional series with Mn, the dependence of the transition temperature is not so obvious. For $e/a > 7.8$, transition temperature decreases with the increase of e/a [15, 16]. However, for $e/a < 7.8$ there is not a clear tendency. Moreover, it has been found that at $e/a = 7.8$, the structural transition

✉ José-María Martín-Olalla
  olalla@us.es

1   Departamento de Física de la Materia Condensada, Facultad de Física, ICMSE-CSIC Universidad de Sevilla, Avenida de la Reina Mercedes s/n, ES41010 Sevilla, Andalucía, Spain

2   Instituto de Ciencia de Materiales de Sevilla, ICMSE-CSIC Universidad de Sevilla, Américo Vespucio 49, ES41092 Sevilla, Andalucía, Spain

temperature and both Curie temperatures of the austenite and the martensite phases are close to room temperature [12], which could make this system candidate for room temperature applications. Therefore, it is of the most interest to perform precise analyses of the martensitic transformation of this system.

Low temperature martensitic transformations are characterized by a very fast diffusionless growth that can be detected by magnetic measurements [17, 18], thermal measurements [19–21], XRD-*in situ* techniques [22], and electrochemical impedance [23]. The diffusionless growth can be described as an autocatalytic kinetic process (e.g., for NiFeGa [24] and NiMnIn Heusler alloys [25]) and yields local symmetry changes that are transmitted to the surrounding at the speed of sound. MT is known to occur intermittently [26–28], due to the existence of kinetic impediments, such as lattice defect, impurities or self-generated heterogeneities that produce a complex energy landscape with different metastable states—multiple minima separated by high energy barriers—in the region of coexistence of the high-symmetry and the low-symmetry phases. If the energy barriers are large enough, the transition only happens when the system is externally driven (athermal transition), so that the transition extends over a finite interval temperature. The strain energy can be stored in the lattice elastically and blocks subsequent growth of the new phase. The transition happens by a succession of strain relaxations between metastable states and avalanches are linked to these fast relaxation processes.

The detection of avalanches has traditionally required the use of experimental techniques sensitive to the strain jumps that occur during relaxation such as acoustic emission [27]; magnetic Barkhausen emission has also provided results in this field [29–31]. Alternatively, calorimetric techniques have proven able to detect and measure the energy associated with the avalanches, which are observed as spikes in DTA traces of high-resolution conduction calorimetry [18, 21, 32, 33] and in differential scanning calorimetry (DSC) traces [34–36]. These techniques provide a straightforward identification of the characteristic energies involved in the jerky events at the prize of more challenging experimental conditions.

In this work, an arc-melted $Ni_{55}Fe_{19}Ga_{26}(e/a = 7.8)$ Heusler alloy is thermally analyzed before and after a thermal treatment, which leads to the formation of a modulated 14M martensite phase from a previous tetragonal martensite phase $L1_0$. The characteristic jerky behavior observed in single crystals [35] is reproduced in the arc-melted polycrystalline sample after the thermal treatment, with events distributed according to a power-law with an exponential cutoff. The characteristic

damping energy is smaller (higher damping) in the reverse transformation.

Experimental

An alloy with nominal, atomic composition $Ni_{55}Fe_{19}Ga_{26}$ was prepared from a mixture of high-purity constituent elements (> 99.9%) in argon atmosphere in an arc furnace MAM-1 (Edmund Bühler GmbH). In order to keep the final composition as close as possible to the nominal one, an additional amount of 2% excess of Ga was added to compensate losses connected with its evaporation during fabrication process (melting temperature 303 K). To obtain a high chemical homogeneity, the alloy was arc-melted several times inside the furnace. Then, parts of the obtained ingot were cut and annealed at 1073 K inside a quartz tube under Ar pressure, adding some Zr wires as getter to prevent oxidation. After an annealing time of 24 h, the quartz tube was quenched in water.

The chemical composition of the original ingot was analyzed by X-ray fluorescence (XRF) using an EAGLE III instrument with an anticathode of Rh.

The average composition of the sample was determined by XRF, obtaining an actual chemical composition (atomic percentage) of $Ni_{54.6}Fe_{19.4}Ga_{26}$. The averaged chemical composition is very close to the nominal one, with a small depletion of Ni and a small enrichment of Fe. Based on the XRF measurements and on the electronic configuration of the outer shells for each element—Ni ($4s^23d^8$), Fe ($4s^23d^6$), and Ga ($4s^24p$)—we estimated the electron valence concentration per atom as $e/a = 7.79$.

The crystal structure was investigated by X-ray diffraction (XRD, Bruker D8 I diffractometer) using Cu K-alpha radiation. Bruker DIFFRAC.EVA (phase identification) and DIFFRAC.TOPAS (Le Bail refinement) software were employed in order to analyze the XRD patterns. Scanning electron microscopy (SEM) was used to study the microstructural features in a FEI Teneo microscope, using secondary electron (SE), backscattered electron (BSE) modes and energy-dispersive X-ray analysis (EDS) to determine the local composition of the different phases. Before the observation in the microscope, the samples were bonded in an epoxy resin and polished.

Thermal properties were studied in a conduction calorimeter described elsewhere [37, 38], which can record high-resolution DTA traces. For this purpose, the measurement device consists of two fluxmeters, with 48 chromel-constantan thermocouples each, which are disposed electrically in series and thermally in parallel. The signal provided by the fluxmeters E is recorded by a Keithley 182 nanovoltmeter at a sampling rate of 12.5 Hz and is converted into a heat flux ϕ by scaling it with a

sensitivity determined in a calibrating experiment [39]. If the rate of temperature change is β then the ratio ϕ/β is the heat exchanged by the sample and the calorimetric block per unit change of temperature. After removing a suitable baseline, any excursion of this quantity is associated with the enthalpy change in the event of phase transition [40–42]. The system operates then as high-resolution differential thermal analyzer with a sensitivity around $1\mu W$. The device is surrounded by a large thermal bath whose temperature is controlled by a Julabo FP40 or FP45 through a heat exchanger coil. Due to the large thermal inertia of the equipment, the scanning rates range from a few kelvin per hour to few milli-kelvin per hour, much slower than commercial differential scanning calorimeters DSC.

The magnetic properties of the $Ni_{55}Fe_{19}Ga_{26}$ system were previously studied in Ref. [12].

Results

Structural and microstructural characterization

Figure 1 depicts XRD patterns at room temperature of the as-prepared bulk sample (ASB) and after annealing treatment and subsequently quenched in water (Thermally Treated Bulk sample, TTB). It has been found that ASB sample reveals the mixture of a non-modulated martensite $L1_0$ tetragonal structure (space group $I4/mmm$) with traces of a γ−phase (space group $Pm\bar{3}m$). This result confirms the limitation of arc-melting technique to produce monophasic compounds. The tetragonal non-modulated martensite, NM, in the ASB sample is replaced by a modulated structure after thermal treatment and subsequent quenching. *Ab initio* calculations suggest that the NM structure is thermodynamically more stable than the 14 M structure [43]. Therefore, the thermal stress, excess of vacancies, etc., induced by the quenching process help to form the non-thermodynamically stable 14 M structure at room temperature, which is typically found in Heusler alloys prepared by rapid quenching techniques [44].

In order to evaluate the modulated character of the martensite phase, a Le Bail refinement, which does not require the full crystal structure data but only the space group of the phases, has been performed on the XRD pattern corresponding to the TTB sample (see Fig. 1b) with GOF = 2.03. The modulated structure can be indexed with the monoclinic space group, obtaining lattice parameters $a = 0.44553(3)\,nm$, $b = 3.0329(3)\,nm$, $c = 0.56195(3)\,nm$ and monoclinic angle equal to $88.009(7)°$. The relation $b = 7a$ indicates a sevenfold increase in the unit cell length along the b axis, coherently with a modulation 14 M. We
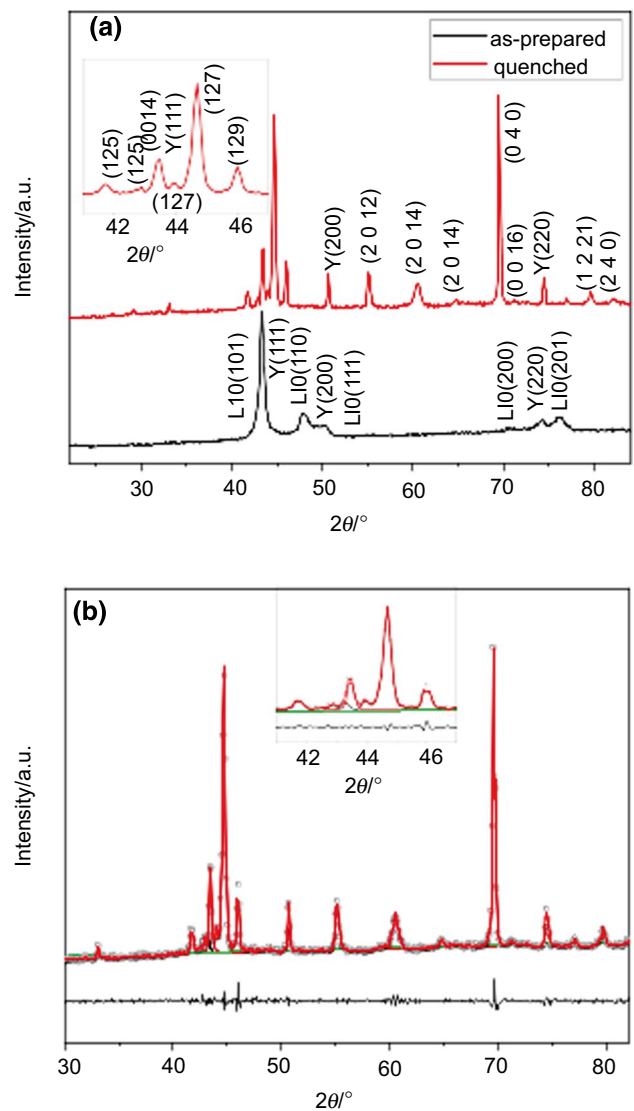

Fig. 1 a XRD patterns of $Ni_{55}Fe_{19}Ga_{26}$ as-prepared (ASB) and quenched bulk (TTB) samples. The Bragg peaks of the modulated phase have been labeled according to the notation of the monoclinic system that usually describes the modulated 14 M structure. **b** XRD pattern of the TTB (open circles) and its Le Bail fitting using martensite phase and γ−phase space groups (red line). The difference is shown at the bottom (black line). The inset depicts a horizontally zoomed plot

obtained a lattice parameter $a = 0.36053(3)\,nm$ for the cubic structure corresponding to the γ−phase.

The microstructure and chemical composition of prepared samples have been analyzed by SEM. Figure 2 shows —panels a and d—the representative SEM secondary electron images of the polished samples. A small black dot in the panel d corresponds to pores created during the fabrication process. The existence of gamma precipitates dispersed inside the martensite grains can be inferred from the SE images, which are clearly observed in the
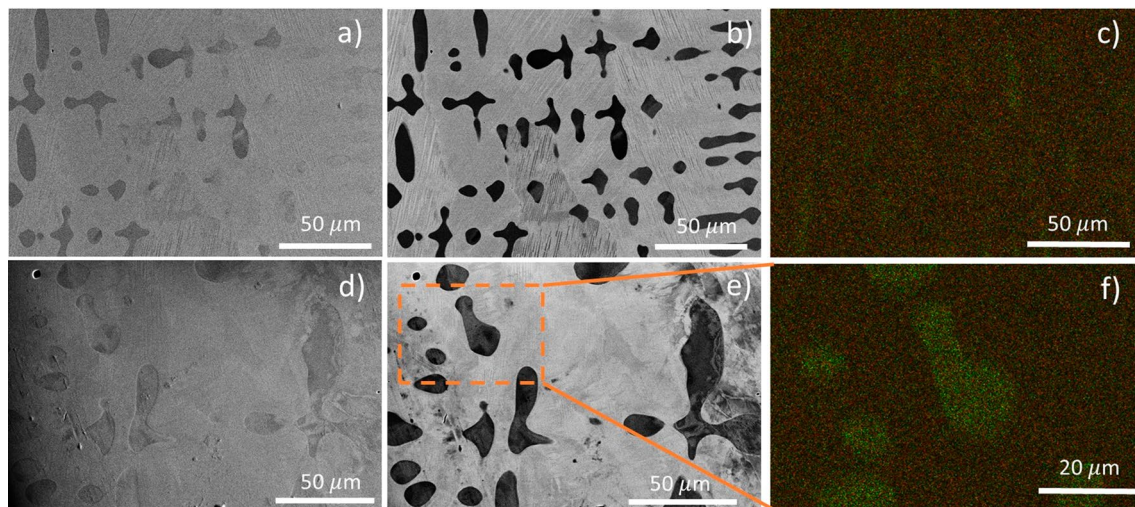
Fig. 2 SEM micrographs obtained using SE—**a** and **d**—and BSE—**b** and **e**—and corresponding compositional maps obtained by EDS—**c** and **f**—. **a–c** correspond to the ASB sample; and **d–f** refers to the TTB sample. Ni, Fe and Ga elements are represented in orange, green and blue, respectively. The dashed area in **e** is magnified in **f**. (Color figure online)

Table 1 Chemical composition (atomic %) for the bulk samples obtained from EDS

Sample	Martensite phase			γ−phase		
	Ni	Fe	Ga	Ni	Fe	Ga
ASB	56 ± 2	19 ± 3	25 ± 3	56 ± 2	26 ± 3	18 ± 3
TTB	56 ± 2	19 ± 3	25 ± 3	57 ± 2	27 ± 3	16 ± 3

case of the backscattered images. The observation of the precipitates, which exhibit a larger size in the case of the TTB sample, is consistent with the XRD analysis reported above.

The EDS elemental mappings of the produced samples are depicted in Fig. 2—c and f, in which the signals of the Ni, Fe and Ga elements are recorded. Table 1 lists the composition of the martensite and γ−phases obtained by EDS point analysis of representative micro-areas of the samples. Despite the thermal treatment of the sample, which leads to the transformation from the non-modulated to the modulated martensitic structure, martensite phase maintains a stable composition. Accordingly, the same results have been obtained for the γ−phase, which is slightly enriched in Fe and depleted in Ga compared to the surrounding martensite matrix.

DTA traces

The ASB sample with dimensions $9.0 \, \text{mm} \times 9.57 \, \text{mm} \times 2.35 \, \text{mm}$ (length × width × height) and $m = 1.5987(1)$ g in mass was placed in the conduction calorimeter to characterize its thermal properties. Thereafter, the sample was removed from the calorimeter, quenched and

transformed into the TTB sample and was placed back in the calorimeter.

In the calorimeter the ASB sample was heated up to 335K, in the austenite phase. Then, the Julabo controller was set to 300 K and the sample was cooled down against this fixed setpoint; the martensitic transformation took place. Thereafter, the sample ASB was further cooled down to 270K and heated back against a fixed setpoint of 340K, while the reverse transformation took place. A similar experiment was carried out for the TTB sample. The rate of temperature change in these runs was around $1 \, \text{K h}^{-1}$ (some $0.015 \, \text{K h}^{-1}$), much slower than the rates in conventional DSC. We will refer this as a slow rate.

Figure 3a shows the excesses of the DTA traces in a cooling (blueish) and a heating (reddish) runs. The exothermic and endothermic excursions correspond to the direct (cooling) and reverse (heating) martensitic transformation.

Table 2 lists the start and finish temperatures—determined form the deviations of the DTA trace— and the peak temperatures. The direct transformation attained the maximum DTA tracte at $M_\text{p} = 322.7$ K, and the reverse transformation, at $A_\text{p} = 329.8$ K, for the ASB sample. On the other hand, the TTB showed cooler peak temperatures $M_\text{p} = 313.1$ K and $A_\text{p} = 319.6$ K, in agreement with Ref. [12]. The TTB sample also showed narrower anomalies

Fig. 3 The DTA traces (top, **a**) and the corresponding evolution of the enthalpy excesses (bottom, **b**) for the slow runs ($\beta \sim 1 \, \text{K h}^{-1}$) on a $Ni_{55}Fe_{19}Ga_{26}$ bulk sample. The vertical axis displays excess heat per unit rate of temperature change and per unit mass (**a**) and excess enthalpy per unit mass (**b**). The ASB runs are shown in lighter shades; the TTB runs in darker shades pale. Blue is used for the direct, cooling, exothermic transformations, red for the reverse, heating, endothermic transformations. Start, finish and peak temperatures are listed in Table 2. The insets zoom in the peak of the DTA anomaly to highlight the rough behavior of the direct transformation in the ASB (**c**) and TTB (**d**) samples. The peak temperatures and the total enthalpy excesses are listed in Table 2. (Color figure online)
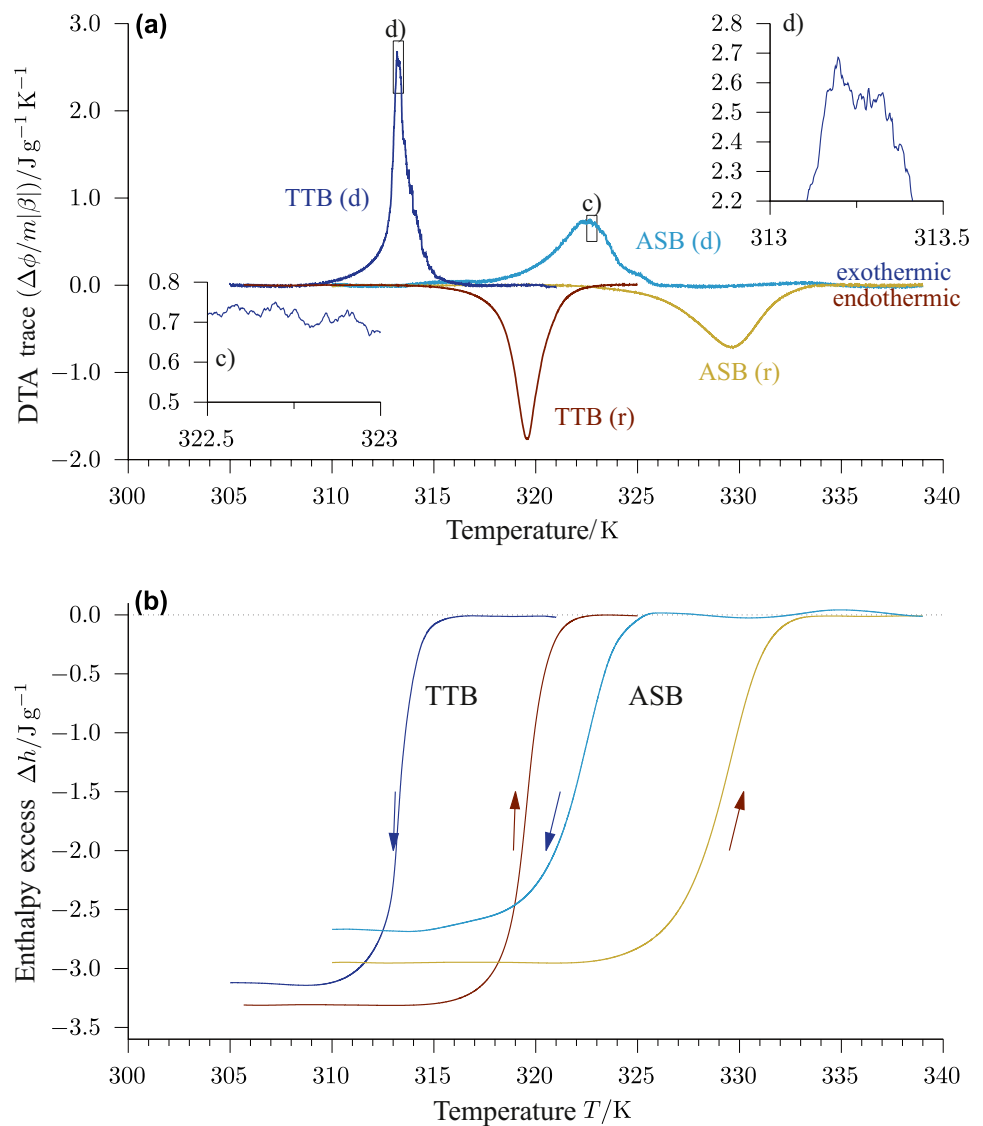
Table 2 Start (*s*), peak (*p*), and finish (*f*) temperatures for the martensite (direct) transformation (*M*) and the austenite (reverse) transformation (*A*) in the $Ni_{55}Fe_{19}Ga_{26}$ bulk sample without (ASB) and with (TTB) thermal treatment

	M_s/K	M_p/K	M_f/K	A_s/K	A_p/K	A_f/K	Δh_d/J g^{-1}	Δh_r/J g^{-1}
ASB	327	322.7	315	322	329.8	335	−2.7	−2.9
TTB	317.3	313.1	308.4	314.2	319.6	323.6	−3.1	−3.3

The transition enthalpies $\Delta h = h_{low} - h_{high}$ for the direct (cooling) and reverse (heating) transformation are also displayed. See Fig. 3 for the DTA traces from which these data originated

and smaller thermal hysteresis $A_p - M_p = 7.1 \, \text{K}$ (ASB) vs $A_p - M_p = 6.5 \, \text{K}$ (TTB). Thermal hysteresis was much smaller than previously reported values [12, 16] ($\sim 25 \, \text{K}$) for experiments carried out at 1000 times faster rates of temperature change.

Both cooling runs showed a distinct rough behavior in the upper half of the direct transformation (see the insets I1 and

I2 in Fig. 3), which was absent in the reverse transformation. This is evidence of a jerky behavior in the direct transformation that will be later analyzed.

The total enthalpy change ($\Delta h = h_{low} - h_{high}$) in either transformation is also listed in Table 2. For the ASB sample we found $\Delta h_d = -2.7 \, \text{Jg}^{-1}$ (direct) and $\Delta h_r = -2.9 \, \text{Jg}^{-1}$ (reverse). For the TTB sample, the excesses increased

by 20% to $\Delta h_d = -3.1 \, \text{Jg}^{-1}$ and $\Delta h_r = -3.3 \, \text{Jg}^{-1}$. These results are inline with those in Ref. [12] (see Fig. 7). The evolution of the partial integration as a function of the temperature is shown in Fig. 3b.

Avalanches

The scanning rates of the previous experiments were much smaller than conventional DSC scans. The DTA cooling traces showed a distinct rough behavior which is magnified in the insets of Fig. 3. This is the result of the coalescence of a myriad of fast, microscopic exchanges, called jerks or avalanches that characterize the martensitic transformation. In our experiment, they occurred in a short scale of time compared to the scale of time of the experiment. Moreover, the insets of Fig. 3 show 10 times larger excursions in the TTB sample. In Discussion, we will develop arguments that link this behavior to the distribution of $\gamma-$phase in either sample.

The jerks or avalanches characterize, at the macroscopic scale, the energies associated with the intermittent dynamic of the phase transition as shown by acoustic emission measurements [26], calorimetry [34, 45] and by high precision calorimetry [18, 21, 32, 33]. They are best analyzed in the adiabatic limit, when the thermal driving is slow enough to prevent overlapping. In that circumstances events are individualized, and their distribution is physically meaningful. Therefore, ultraslow experiments were conducted on the TTB sample following the strategy of Romero et al. [46]. Now the rate of temperature change was controlled by the Julabo FP45 and was set to $\beta_2 = \pm 40 \, \text{mK h}^{-1}$, ~ 25 slower than the previous run.

Figure 4 shows an interval of 0.5 K for the slow and the ultraslow runs. The panel a shows the slow cooling run; panel b, the ultraslow cooling run; and panel c), the ultraslow heating run. Notice that in panels a and b the temperature increases from right to left so that in every data set the time goes from left to right. Figure 4 shows the raw signal provided by the fluxmeters at a sampling rate of 12.5 Hz scaled by their sensitivity. In panel c the standard noise of the signal ($\sim 0.3 \, \mu\text{W}$ full height) is evident due to the high magnification of the vertical axis.

In order to characterize the spikes, we smoothed the cooling signal with a fifth-order all-pole Butterworth filter with a cut-off frequency of 1 Hz. On the other hand, the heating signal was resampled at 0.1 Hz by averaging blocks of 125 data points. Thereafter, we identified local maxima and local minima: events when the signal stops
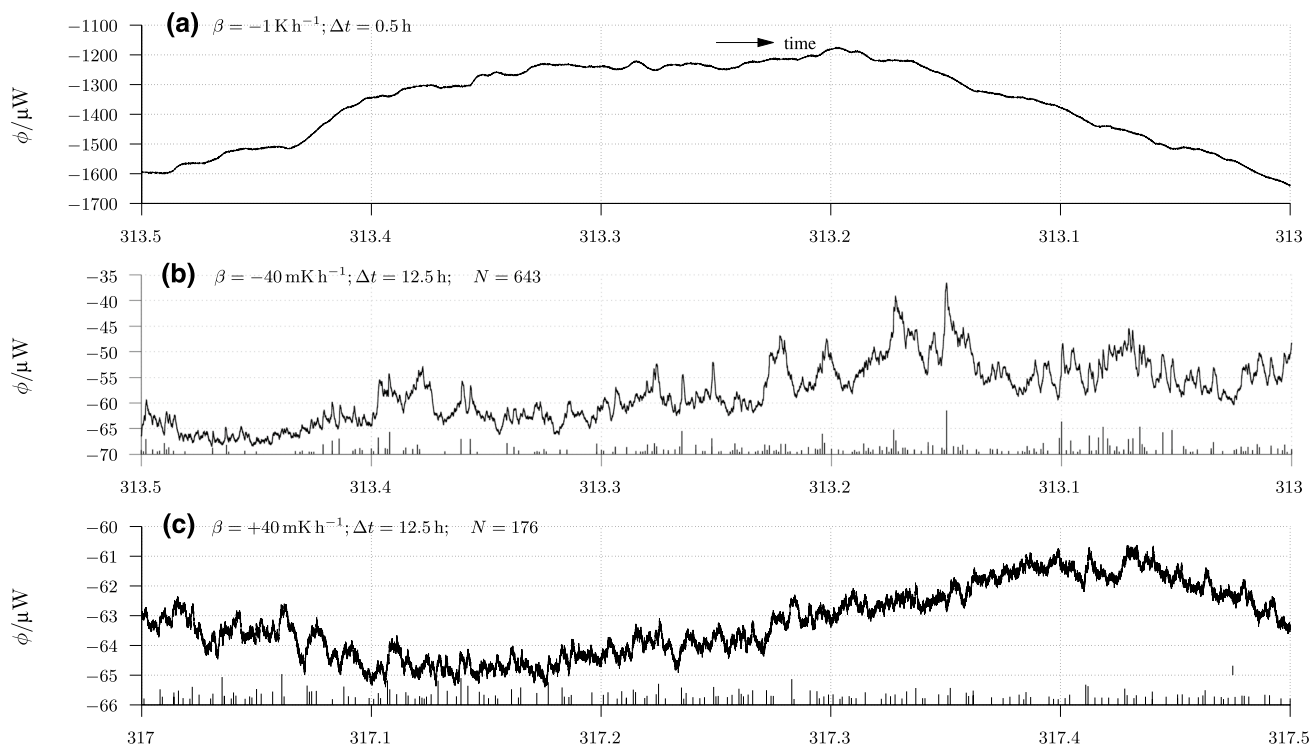

Fig. 4 A close-up of the heat flux for $\beta = -1 \, \text{K h}^{-1}$ (**a**, 0.5 h), $\beta = -40 \, \text{mK h}^{-1}$ (**b**, 12.5 h); and $\beta = +40 \, \text{mK h}^{-1}$ (**c**, 12.5 h). Notice that the $x-$axis is conformed so that the time advances from left to right in every panel. **b**, **c** show only one in every ten data points. The vertical axis in **c** is six times magnified relative to **b**. The top left label in **b**, **c** display the number of jerks higher than 30 nV in the plot. The jerks are located by vertical lines at the horizontal axis. The temperature interval shown in **b**, **c** are those of the highest activity in either run, see Fig. 6

increasing (maxima) or stops decreasing (minima). The size of the event (spike, jerk or avalanche) is associated with the size of a monotonous up rise from one minimum to the following maximum. The energy of the event is determined by scaling the heat flux with the time constant of the calorimeter ($\tau = 70$ s) [21].

We searched for a threshold E_0 such that events larger or equal than E_0 occurred only during the temperature interval of the martensite transformation. Therefore, they can be attributed to the transformation. The threshold was identified at $E_0 = 30$ nV in the raw signal of the voltmeter; $\phi_0 = E_0/\alpha = 0.2\,\mu W$ in the heat flux scale and $u_0 = \phi_0\tau = 13\,\mu J$ in the energetic scale. The top, left label in panels B and C of Fig. 4 shows the number of events larger than the threshold found in the interval.

Figure 5 shows histogram plots of the activity—number of events $E > E_0$ per kelvin—measured along 0.2 K-width bins for either ultraslow run. For the direct (cooling) transformation we collected $N = 1756$ such events with median value 26 μJ; they made $U = 74\,\mu J$, or 1.5% of the total enthalpy. For the reverse transformation we identified $N = 830$ events, with median value 19μJ and making 18 μJ or 0.4% of the total enthalpy.

Finally, we computed the empirical cumulative complementary distribution function (empirical CCDF): the shares of avalanches larger or equal than a given size. The empirical CCDF was determined by ranking the avalanches from the largest (rank one) to the smallest (rank N, assigned to u_0). Then, the empirical CCDF is the ratio of the rank to the sample size. Figure 6 shows the empirical CCDF against the avalanche size u in the energetic scale for the direct (dark blue) and reverse (dark red) transformation. The empirical CCDF shows a quasi-linear behavior in the $\log - \log$ plot, indicating a power

Fig. 5 Histogram plot showing the activity—number of events per kelvin—derived from the number of events larger than $u_0 = 13\,\mu J$ observed in a 0.2 K interval for the ultraslow experiments. The bluish histogram shows the direct (cooling) run; the reddish histogram shows the reverse (heating) run. The x−axis shows the austenite and martensite start and finish temperatures, see Table 2
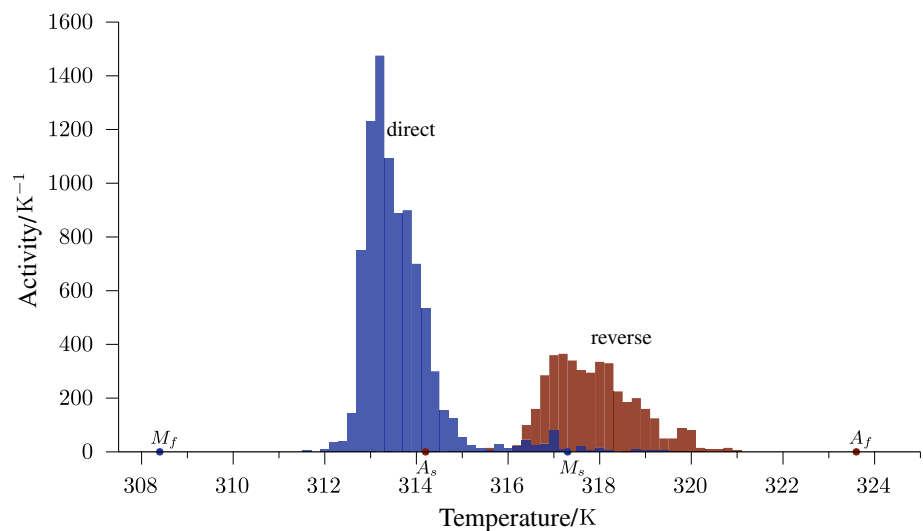

Fig. 6 The energetic distributions of avalanche sizes for the ultraslow runs in the direct (dark blue) and reverse (dark red) transformations. The vertical axis displays the empirical complementary distribution function (ECCDF). The horizontal axis displays the energetic size of the avalanche. The quasilinear behavior in the $\log - \log$ scale suggests a power law distribution with exponent ε in the range (2, 3). The lack of very large energetic sizes suggests an exponential cutoff with characteristic energy $\hat{\xi}$. (Color figure online)
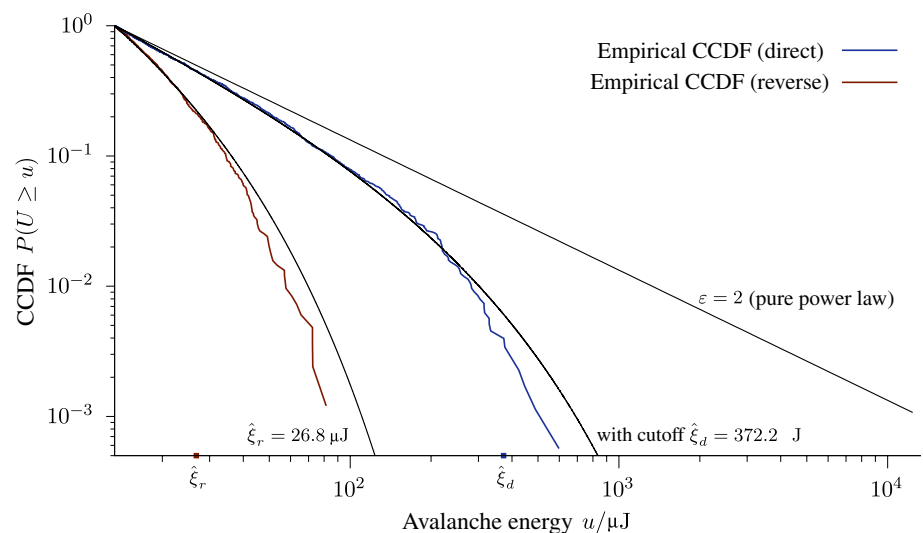
law distribution of events $p(u) \propto u^{-\varepsilon}$, where the larger avalanches are increasingly scarce.

Notably, as observed in Fig. 4 and in Fig. 3, the size of the largest avalanches during the reverse transformation is one order of magnitude smaller than those observed during the direct transformation.

These results show different behavior in the direct and reverse transformations with greater activity, larger sizes and smaller exponent in the direct experiment. These differences have already been reported and studied in martensitic transformations [33, 45, 47]. In Sect. 4, we will further discuss this issue.

Discussion

Aside from the development of the 14 M martensite phase, the main effect of thermal treatment is the coarsening of the γ−phase and the austenite crystals, which alter the differences between the direct and reverse transformations [35]. In Fig. 2, this is evidenced by the increase in the distances between γ−phase crystals.

The intermittent dynamics of the direct and the reverse transitions in martensitic transformations are characteristically asymmetric: exponents and accumulated energy differ in either transformations. This has been previously associated with the fact that nucleation is required in the direct transformation, whereas the reverse transformation occurs by fast shrinkage of martensitic domains [47]. Alternatively, the different mechanism of the relaxation of elastic strain energy in either transition was proposed as a source of the asymmetry [45]. The asymmetry manifests itself even in the adiabatic conditions, see here Figs. 4–6, see also Ref. [33], which put forward the intrinsic nature of the phenomenon. Analytically, the slope of the CCDF at the top of the distribution characterizes the asymmetry. Our results in Fig. 6 show $\varepsilon \sim 2.3$ (direct) and $\varepsilon \sim 3$ (reverse). Either case the exponents are larger than $\varepsilon = 2$, expected for monoclinic to cubic transformation [48] and larger that the exponents reported previously on a NiFeGaCo sample from DSC cooling measurements ($\varepsilon \sim 1.9$), see Ref. [35, 49].

Planes and Vives [47] using acoustic emission characterized the asymmetry in, among others, Cu–Zn–Al shape-memory alloy single crystals, which undergoes a cubic to monoclinic phase transition. They reported different exponents for the direct and reverse transformation and different distributions of energy sizes—power law (direct) and power law with exponential cutoff (reverse)—from a maximum likelihood analysis of the empirical observations. The analysis included a bidimensional chart of ε, ξ for several choices of $E_{\min}$.

Inspired by this analysis, and considering that the grain boundaries must stop the growing of avalanches, we tested the distribution of calorimetric events against a power law with exponential cutoff for events larger than u_0 (see also Ref. [50]). The model is characterized by an exponent ε and a damping energy ξ which further hinders the probability of observing large events: $p(u; \varepsilon, \xi) \propto u^{-\varepsilon} \times \exp(-u/\xi)$. For our analysis, we derived the empirical complementary cumulative distribution function ECCDF for the N observed events larger than u_0 (see Sect. 3.3). On the other hand, we set an array 200×200 of ε_i, ξ_j pairs and computed:

$$\mathrm{CCDF}(u; \varepsilon_i, \xi_j) = \frac{\int_u^\infty t^{-\varepsilon_i} \times \exp(-t/\xi_j)dt}{\int_{u_0}^\infty t^{-\varepsilon_i} \times \exp(-t/\xi_j)dt}, \tag{1}$$

by numerical integration. The ε values were arranged linearly from 1 to 2.5 (direct) and 1 to 3.5 (reverse); while the ξ values were logarithmically arranged from $10^{0.5}u_0$ to $10^3 u_0$.

Finally, we computed the Kolmogorov–Smirnov distance given by the maximum absolute distance between the two, empirical and model, CCDF:

$$D(\varepsilon_i, \xi_j) = D_{ij} = \sqrt{N} \times \max(|\mathrm{ECCDF}(u) - \mathrm{CCDF}(u; \varepsilon_i, \xi_j)|). \tag{2}$$

The Kolmogorov–Smirnov distance provides a p value for the null hypothesis "the empirical distribution originates from the tested model": at the standard level of confidence $\alpha = 0.05$ the null hypothesis sustains when D is below $D_0 = 1.358$ [51].

Figure 7a shows the bi-dimensional grid ε, ξ and, by the color depth, the Kolmogorov–Smirnov distance D_{ij}. The heatmap highlights the region where $D_{ij} < 2$: darker shades show smaller Kolmogorov–Smirnov distance and therefore greater similarity between the empirical distribution and the tested model.

The heatmap shows that for pure power law analysis— that is $u_0/\xi \to 0$—the exponent goes to ~ 2.3 (direct) and ~ 3 (reverse), as noted earlier. Understandably, a finite damping energy yields a smaller exponent in the power law component. The inset b shows the relationship between $\min(D_{ij})$ and ε for the direct (solid blue circles) and the reverse (open red circles) transformations. The dashed line signals D_0 and, remarkably, both transformations sustain values below D_0 for $\varepsilon \sim 2$. The inset c shows the distribution of D_{ij} as a function of ξ at the condition $\varepsilon = 2$. The local minimum $\hat{\xi}$ for either transformation can easily be spotted; they differ roughly in one order of magnitude.
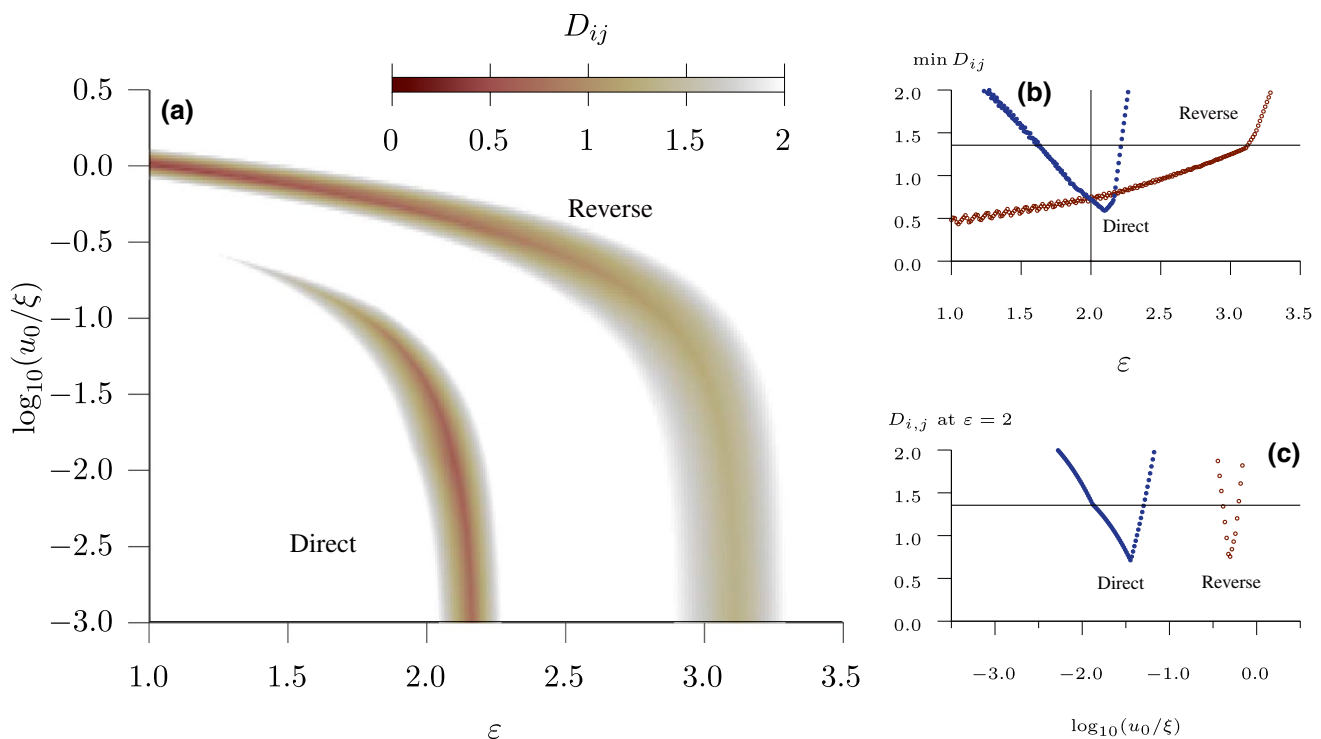
Fig. 7 The Kolmogorov–Smirnov distance (color depth) from the empirical CCDF to the CCDF of a biparametric power-law distribution with exponential cutoff (**a**). The parameters of the model are represented in the x–axis (exponent) and y–axis (damping energy) in a 200×200 grid. The inset **b** shows $\min(D_{ij})$ as a function of ε. The inset **c** shows D_{ij} as a function of ξ for the condition $\varepsilon = 2$, representa-tive of the cubic to monoclinic transformation. Either inset shows the direct transformation by solid blue circles and the reverse transformation by open red circles. Notice that either transformation attains similar, low values of D_{ij} at $\varepsilon = 2$ (**b**), whereas the damping parameter differs in one order of magnitude (**c**), see also Fig. 6

Table 3 Deduced upper boundaries (black) and reported values (bold) for $\log_{10}(u_0/\xi)$ in acoustic emission (AE) jerks and calorimetric jerks for system that undergo cubic to monoclinic martensitic transitions

| System | $\log_{10}(u_0/\xi)$ | | | |
| | AE | | Calorimetry | |
	Direct	Reverse	Direct	Reverse
Cu–Zn–Al [21, 47]	− 2.0	**− 2.5**	− 1.3	− 1.3
Cu–Al–Be [33]	− 5.0	**− 2.0**	− 2.5	**− 1.0**
Ni–Fe–Ga–Co [35]	− 4.5	− 3.0	− 2.0	n.a.
Ni–Mn–In [18]	− 3.0	− 3.0	− 3.0	− 3.0
Ni–Fe–Ga (this work)			**− 1.5**	**− 0.3**

The boundaries are given by $\log_{10}(u_0/u_{\max})$ when pure power-law is reported. It provides a lower bound since ξ must be larger than $u_{\max}$. The rate of temperature change in AE experiments was usually in the range of several kelvin per minute. Calorimetric experiments were carried out in DSC calorimetry [35] at similar rates, and in conduction calorimetry (otherwise) at ultraslow rates.

Light numbers reproduce deduced lower bounds; bold numbers, reported values

In summary a power-law with exponent $\varepsilon = 2$ and an appropriate damping energy suffices to describe the distribution of events both in the direct and in the reverse transformation; the ratio $\Xi = \hat{\xi}_d/\hat{\xi}_r \sim 14$ of the damping energies characterizes the asymmetry in the transformation. Figure 6 also shows the CCDF for these choices of $\varepsilon = 2, \hat{\xi}$ in either transformation (dashed lines), compared with the empirical distribution and the pure power-law behavior.

Table 3 lists reported values from a set of previous AE and calorimetry studies. Pure power-law reports correspond to $\xi \to \infty$, but the study is always limited by the largest event in the catalog $u_{\max}$. Eventually the largest event is an experimental lower bound for ξ. The table reproduces this deduced lower bounds in light, and reported values of ξ in bold. Values are shown as $\log_{10}(u_0/\xi)$.

In our case, we hypothesize that the arc melting technique followed by the thermal treatment has resulted in larger presence of local free energy barriers that lead to intermittent dynamics and asymmetry, as well as eventually prevented the growing of larger avalanches thus giving rise to a smaller, finite $\hat{\xi}$. Our estimate is some ten times smaller than results extracted from Ref. [35].

On the other hand, if the transition mechanisms were associated with an elastic, surface energy [45] then $\sqrt{\Xi} \sim 4$ would be a rough estimate of the ratio in the longitudinal size of the surface driving the avalanches. Alternatively, if they were associated with martensite phase developed in an austenite crystal [47], $\sqrt[3]{\Xi} \sim 2.5$ would be a rough estimate of the longitudinal size of the characteristic volume driving the avalanches. Furthermore, in this case, a rough estimation of an upper bound for the volume of sample affected in a single event can be obtained from the following argument. We first take the total specific energy of the transformation ($|\Delta h| \sim 3 \text{J g}^{-1}$, see Table 2), the sample mass m and the sample volume V (see Sect. 2). Then, the volume size of an event e is proportional count $v = Ve/|\Delta h|m$ and the diameter of a sphere of equal volume is $d = 6(Ve/|\Delta h|m)^{1/3}/\pi$. For the median value of the event distribution—$\langle e_\text{d} \rangle = 26 \, \mu\text{J}$—we get $d \sim 100 \mu$ m which is roughly in agreement with the size of the austenite crystals that can be deduced from Fig. 2 as this grain boundaries should stop the progression of martensite fronts during the transformation and would give rise to $\hat{\xi}_\text{d} = 372.2 \, \mu\text{J}$, equivalent to the volume of a sphere 300 μm in diameter. We note that less than 1% of the recorded events were larger than $\hat{\xi}_\text{d}$. In contrast, the reverse transition which occurs by fast shrinkage of the martensitic domains [47] showed a smaller damping energy $\hat{\xi}_\text{r} = 25 \, \mu\text{J}$, similar to the median value of the event distribution ($\langle e_\text{r} \rangle = 19 \, \mu\text{J}$) and resulted in roughly 20% of the recorded reverse events larger than ξ_r.

Accordingly, the lack of intermittent dynamics in the ASB samples suggests ξ smaller than the observed values in the TTB sample. Understandably, the larger distribution of γ-phase should have further hindered the size of the events and resulted in a smoother distribution, see Fig. 3.

Conclusions

We have thermally characterized a $Ni_{55}Fe_{19}Ga_{26}$ alloy produced by the arc melting technique with and without a posterior thermal treatment that promotes the metastable, adaptative 14 M phase at room temperature.

The thermal treatment narrows the thermal hysteresis and the temperature distance for the start to finish condition. Interestingly, the thermal treatment enhances the intermittent dynamics (avalanches) of the martensite transition both in the direct and in the reverse transformations. The jerky behavior was more prominent in the direct (cubic to 14 M) transformation.

The distribution of avalanches follows a power law with an exponential cutoff both in the direct and reverse transformation. The exponent $\varepsilon = 2$ associated with the cubic to monoclinic transformation suffices to explain the power law decay both in the direct and reverse transformations.

This result is in line with previous observations. We identified the damping energies associated with the transformations and found that the reverse transformation is 10 times more damped than the direct transformation. This is a quantification of the asymmetry of the processes involved in the transformation.

Declarations

References

1. Zhang JX, Sato M, Ishida A. Deformation mechanism of martensite in Ti-rich Ti–Ni shape memory alloy thin films. Acta Mater. 2006;54:1185–98. https://doi.org/10.1016/J.ACTAMAT.2005.10.046.

2. Fan G, Chen W, Yang S, Zhu J, Ren X, Otsuka K. Origin of abnormal multi-stage martensitic transformation behavior in aged Ni-rich Ti–Ni shape memory alloys. Acta Mater. 2004;52:4351–62. https://doi.org/10.1016/J.ACTAMAT.2004.06.002.

3. Thamburaja P, Anand L. Superelastic behavior in tension-torsion of an initially-textured Ti–Ni shape-memory alloy. Int J Plast. 2002;18:1607–17. https://doi.org/10.1016/S0749-6419(02)00031-1.

4. Khalil ANM, Azmi AI, Murad MN, Ali MAM. The effect of cutting parameters on cutting force and tool wear in machining nickel titanium shape memory alloy ASTM f2063 under minimum quantity nanolubricant. Procedia CIRP. 2018;77:227–30. https://doi.org/10.1016/J.PROCIR.2018.09.002.

5. Canbay CA, Aydogdu A. Thermal analysis of cu-14.82 wt pct al-0.4 wt pct be shape memory alloy. J Therm Anal Calor. 2013;113:731–7. https://doi.org/10.1007/S10973-012-2792-6.

6. Silva DDS, Guedes NG, Oliveira DF, Torquarto RA, Júnior FWELA, Lima BASG, Feitosa FRP, Gomes RM. Effects of long-term thermal cycling on martensitic transformation temperatures and thermodynamic parameters of polycrystalline cualbecr shape memory alloy. J Therm Anal Calorim. 2022;147:7875–81. https://doi.org/10.1007/S10973-021-11106-5.

7. Pedrosa MTMA, Silva DDS, Brito ICA, Alves RF, Caluête RE, Gomes RM, Oliveira DF. Effects of hot rolling on the microstructure, thermal and mechanical properties of cualbenbni shape memory alloy. Thermochim Acta. 2022;711: 179188. https://doi.org/10.1016/J.TCA.2022.179188.

8. Ullakko K, Huang JK, Kantner C, O'Handley RC, Kokorin VV. Large magnetic-field-induced strains in ni2mnga single crystals. Appl Phys Lett. 1996;69:1966–8. https://doi.org/10.1063/1.117637.

9. Planes A, Mañosa L, Moya X, Krenke T, Acet M, Wassermann EF. Magnetocaloric effect in Heusler shape-memory alloys. J Magn Magn Mater. 2007;310:2767–9. https://doi.org/10.1016/J.JMMM.2006.10.1041.

10. Bachaga T, Zhang J, Khitouni M, Sunol JJ. NiMn-based heusler magnetic shape memory alloys: a review. Int J Adv Manuf Technol. 2019;103:2761–72. https://doi.org/10.1007/S00170-019-03534-3.

11. Maziarz W, Wójcik A, Grzegorek J, Zywczak A, Czaja P, Szczerba MJ, Dutkiewicz J, Cesari E. Microstructure, magneto-structural transformations and mechanical properties of Ni50Mn37.5Sn12.5-$x$in$x$ ($x = 0, 2, 4, 6$ at pct) metamagnetic shape memory alloys sintered by vacuum hot pressing. J Alloy Compd. 2017;715:445–53. https://doi.org/10.1016/J.JALLCOM.2017.04.280.

12. Manchón-Gordón AF, Ipus JJ, Kowalczyk M, Blázquez JS, Conde CF, Švec P, Kulik T, Conde A. Comparative study of structural and magnetic properties of ribbon and bulk Ni55Fe19Ga26 Heusler alloy. J Alloy Compd. 2021;889: 161819. https://doi.org/10.1016/J.JALLCOM.2021.161819.

13. Moya X, Mañosa L, Planes A, Krenke T, Acet M, Wassermann EF. Martensitic transition and magnetic properties in Ni–Mn–x alloys. Mater Sci Eng, A. 2006;438–440:911–5. https://doi.org/10.1016/J.MSEA.2006.02.053.

14. Pons J, Cesari E, Seguí C, Masdeu F, Santamarta R. Ferromagnetic shape memory alloys: Alternatives to Ni–Mn–Ga. Mater Sci Eng, A. 2008;481–482:57–65. https://doi.org/10.1016/J.MSEA.2007.02.152.

15. Yu HJ, Fu H, Zeng ZM, Sun JX, Wang ZG, Zhou WL, Zu XT. Phase transformations and magnetocaloric effect in NiFeGa ferromagnetic shape memory alloy. J Alloy Compd. 2009;477:732–5. https://doi.org/10.1016/J.JALLCOM.2008.10.143.

16. Sarkar SK, Biswas A, Babu PD, Kaushik SD, Srivastava A, Siruguri V, Krishnan M. Effect of partial substitution of Fe by Mn in Ni55Fe19Ga26 on its microstructure and magnetic properties. J Alloy Compd. 2014;586:515–23. https://doi.org/10.1016/J.JALLCOM.2013.10.057.

17. Recarte V, Pérez-Landazábal JI, Sánchez-Alarcos V, Rodríguez-Velamazán JA. Dependence of the martensitic transformation and magnetic transition on the atomic order in Ni–Mn–In metamagnetic shape memory alloys. Acta Mater. 2012;60:1937–45. https://doi.org/10.1016/J.ACTAMAT.2012.01.020.

18. Romero FJ, Martín-Olalla J-M, Blázquez JS, Gallardo MC, Soto-Parra D, Vives E, Planes A. Thermo-magnetic characterization of phase transitions in a Ni–Mn–In metamagnetic shape memory alloy. J Alloy Compd. 2021;887: 161395. https://doi.org/10.1016/J.JALLCOM.2021.161395.

19. Bouabdallah M, Cizeron G. Caracterisation par dsc des sequences de transformation au cours d'un chauffage lent des alliages amf a base de Cu–Al–Ni. J Therm Anal Calorim. 2002;68:951–6. https://doi.org/10.1023/A:1016146707434.

20. Cesari E, Chernenko VA, Font J, Muntasell J. ac technique applied to cp measurements in Ni–Mn–Ga alloys. Thermochim Acta. 2005;433:153–6. https://doi.org/10.1016/J.TCA.2005.02.029.

21. Gallardo MC, Manchado J, Romero FJ, Cerro JD, Salje EKH, Planes A, Vives E, Romero R, Stipcich M. Avalanche criticality in the martensitic transition of Cu67.64 Zn16.71 Al15.65 shape-memory alloy: a calorimetric and acoustic emission study. Phys Rev B—Condens Matter Mater Physics. 2010;81: 174102. https://doi.org/10.1103/PHYSREVB.81.174102.

22. Czaja P, Przewoznik J, Gondek Hawelek L, Zywczak A, Zschech E. Low temperature stability of 4O martensite in Ni49.1Mn38.9Sn12 metamagnetic Heusler alloy ribbons. J Magn Magn Mater. 2017;421:19–24. https://doi.org/10.1016/J.JMMM.2016.07.065.

23. Cunha MF, Sobrinho JMB, Souto CR, Santos AJV, Castro AC, Ries A, Sarmento NLD. Transformation temperatures of shape memory alloy based on electromechanical impedance technique. Measurement. 2019;145:55–62. https://doi.org/10.1016/J.MEASUREMENT.2019.05.050.

24. Manchón-Gordón AF, López-Martín R, Ipus JJ, Blázquez JS, Svec P, Conde CF, Conde A. Kinetic analysis of the transformation from 14 m martensite to l21 austenite in Ni–Fe–Ga melt spun ribbons. Metals. 2021;11:849. https://doi.org/10.3390/MET11060849.

25. Blázquez JS, Romero FJ, Conde CF, Conde A. A review of different models derived from classical Kolmogorov, Johnson and Mehl, and Avrami (KJMA) theory to recover physical meaning in solid-state transformations. Phys Status Solidi (B). 2022;259:2100524. https://doi.org/10.1002/PSSB.202100524.

26. Vives E, Ortín J, Mañosa L, Ráfols I, Pérez-Magrané R, Planes A. Distributions of avalanches in martensitic transformations. Phys Rev Lett. 1994;72:1694. https://doi.org/10.1103/PhysRevLett.72.1694.

27. Planes A, Mañosa L, Vives E. Acoustic emission in martensitic transformations. J Alloy Compd. 2013;577:699–704. https://doi.org/10.1016/J.JALLCOM.2011.10.082.

28. Salje EKH, Dahmen KA. Crackling noise in disordered materials. Ann Rev Condens Matter Phys. 2014;5:233–54. https://doi.org/10.1146/ANNUREV-CONMATPHYS-031113-133838.

29. Sullivan MR, Shah AA, Chopra HD. Pathways of structural and magnetic transition in ferromagnetic shape-memory alloys. Phys Rev B—Condens Matter Mater Phys. 2004;70: 094428. https://doi.org/10.1103/PHYSREVB.70.094428.

30. Baró J, Dixon S, Edwards RS, Fan Y, Keeble DS, Mañosa L, Planes A, Vives E. Simultaneous detection of acoustic emission and Barkhausen noise during the martensitic transition of a Ni–Mn–Ga magnetic shape-memory alloy. Physical Rev B—Condens Matter and Mater Phys. 2013;88: 174108. https://doi.org/10.1103/PHYSREVB.88.174108/.

31. Tóth LZ, Daróczi L, Szabó S, Beke DL. Simultaneous investigation of thermal, acoustic, and magnetic emission during martensitic transformation in single-crystalline ni2mnga. Phys Rev B. 2016;93: 144108. https://doi.org/10.1103/PHYSREVB.93.144108.

32. Vives E, Baró J, Gallardo MC, Martín-Olalla J-M, Romero FJ, Driver SL, Carpenter MA, Salje EKH, Stipcich M, Romero R, Planes A. Avalanche criticalities and elastic and calorimetric anomalies of the transition from cubic Cu-Al-Ni to a mixture of 18r and 2h structures. Phys Rev B. 2016. https://doi.org/10.1103/PhysRevB.94.024102.

33. Romero FJ, Martín-Olalla J-M, Gallardo MC, Soto-Parra D, Salje EKH, Vives E, Planes A. Scale-invariant avalanche dynamics in the temperature-driven martensitic transition of a Cu–Al–Be single crystal. Phys Rev B. 2019;99: 224101. https://doi.org/10.1103/PhysRevB.99.224101.

34. Blobaum KJM, Krenn CR, Mitchell JN, Haslam JJ, Wall MA, Massalski TB, Schwartz AJ. Evidence of transformation bursts during thermal cycling of a Pu–Ga alloy. Metall Mater Trans A. 2006;37:567–77. https://doi.org/10.1007/S11661-006-0029-7.

35. Bolgár MK, Daróczi L, Tóth LZ, Timofeeva EE, Panchenko EY, Chumlyakov YI, Beke DL. Effect of gamma precipitates on thermal and acoustic noises emitted during austenite/martensite transformation in NiFeGaCo single crystals. J Alloy Compd. 2017;705:840–8. https://doi.org/10.1016/J.JALLCOM.2017.02.167.

36. Kamel SM, Daróczi L, Tóth LZ, Panchenko E, Chumljakov YI, Samy NM, Beke DL. Acoustic emission and DSC investigations of anomalous stress-stain curves and burst like shape recovery of Ni49Fe18Ga27Co6 shape memory single crystals. Intermetallics. 2023;159: 107932. https://doi.org/10.1016/J.INTERMET.2023.107932.

37. Cerro JD, Ramos S, Sanchez-Laulhe JM. Flux calorimeter for measuring thermophysical properties of solids: study of TGS. J Phys E: Sci Instrum. 1987;20:612. https://doi.org/10.1088/0022-3735/20/6/006.

38. Jimenez F, Ramos S, Cerro JD. Specific heat measurement of LATGS crystals under nonequilibrium conditions. Phase Trans. 1988;12:275–84. https://doi.org/10.1080/01411598808207888.

39. Martín JM, Cerro JD, Ramos S. Simultaneous measurement of thermal and dielectric properties in a conduction calorimeter: application to the lock-in transition in Rb2ZnCl4 single crystal. Phase Trans. 1997;64:45–55. https://doi.org/10.1080/01411597098227767.

40. Martín-Olalla JM, Cerro JD, Ramos S. Evidence of latent heat in the Rb2ZnCl4 commensurate-incommensurate phase transition. J Phys: Condens Matter. 2000;12:1715. https://doi.org/10.1088/0953-8984/12/8/314.

41. Cerro JD, Romero FJ, Gallardo MC, Hayward SA, Jiménez J. Latent heat measurement near a tricritical point: a study of the kMnf3 ferroelastic crystal. Thermochim Acta. 2000;343:89–97. https://doi.org/10.1016/S0040-6031(99)00300-7.

42. Romero FJ, Gallardo MC, Czarnecka A, Koralewski M, Cerro JD. Thermal and kinetic study of the ferroelectric phase transition in deuterated triglycine selenate. J Therm Anal Calor. 2007;87(2):355–61. https://doi.org/10.1007/S10973-005-7444-7.

43. Zayak AT, Entel P. Role of shuffles and atomic disorder in Ni–Mn–Ga. Mater Sci Eng: A. 2004;378:419–23. https://doi.org/10.1016/J.MSEA.2003.10.368.

44. Manchón-Gordón AF, Ipus JJ, Kowalczyk M, Wójcik A, Blázquez JS, Conde CF, Maziarz W, Švec P, Kulik T, Conde A. Effect of pressure on the phase stability and magnetostructural transitions in nickel-rich NiFeGa ribbons. J Alloy Compd. 2020;844: 156092. https://doi.org/10.1016/J.JALLCOM.2020.156092.

45. Beke DL, Bolgár MK, Tóth LZ, Daróczi L. On the asymmetry of the forward and reverse martensitic transformations in shape memory alloys. J Alloy Compd. 2018;741:106–15. https://doi.org/10.1016/j.jallcom.2017.11.271.

46. Romero FJ, Manchado J, Martín-Olalla JM, Gallardo MC, Salje EKH. Dynamic heat flux experiments in Cu67.64Zn16.71Al15.65: separating the time scales of fast and ultra-slow kinetic processes in martensitic transformations. Appl Phys Lett. 2011;99: 011906. https://doi.org/10.1063/1.3609239.

47. Planes A, Vives E. Avalanche criticality in thermal-driven martensitic transitions: the asymmetry of the forward and reverse transitions in shape-memory materials*. J Phys: Condens Matter. 2017;29: 334001. https://doi.org/10.1088/1361-648X/AA78D7.

48. Porta M, Castán T, Saxena A, Planes A. Influence of the number of orientational domains on avalanche criticality in ferroelastic transitions. Phys Rev E. 2019;100: 062115. https://doi.org/10.1103/PHYSREVE.100.062115.

49. Bolgár MK, Tóth LZ, Szabó S, Gyöngyösi S, Daróczi L, Panchenko EY, Chumlyakov YI, Beke DL. Thermal and acoustic noises generated by austenite/martensite transformation in NiFeGaCo single crystals. J Alloy Compd. 2016;658:29–35. https://doi.org/10.1016/J.JALLCOM.2015.10.173.

50. Clauset A, Shalizi CR, Newman MEJ. Power-law distributions in empirical data. SIAM Rev. 2009;51:661–703. https://doi.org/10.1137/070710111.

51. Papoulis A, Pillai SU. Probability, random variables and stochastic processes. 4th ed. NY: McGraw-Hill; 2002.